In Situ Observations and Tuning of Physical and Chemical Phenomena on the Surfaces of Strongly Correlated Oxides

Zheng Gai, S. V. Kalinin, An-Ping Li, Jian Shen, and A. P. Baddorf*

The characteristic aspect of strongly correlated oxides systems is the strong coupling between the structural, electronic and magnetic properties. A small change in one property can produce a large change in another. Controllable surface tuning provides the opportunity to study how structural, electronic, and magnetic properties respond to the broken symmetry and opens avenues for exploration of completely new physical properties. The extreme sensitivity of properties to external chemical and physical stimuli makes in situ characterization a requirement for controlled tuning of complex correlated materials. This paper reviews some recent progress in in situ observations and tuning of physical and chemical phenomena on the surfaces of strongly correlated oxides thin films and crystals, including atomic-level structural studies, control, and tuning of the physical properties.

1. Introduction

Strongly correlated oxides have attracted much attention due to a broad gamut of functionalities they exhibit.[1–3] A hallmark of these complex systems is the strong coupling between the structural, electronic and magnetic properties. A small change in one property (e.g., structure) can produce a large change in another property (e.g., the electronic state), enabling a broad range of novel functionalities and applications. The subtle balance between complex phases can be readily shifted by external stimuli, resulting in dramatically new electrical or magnetic properties. Creating a surface by cleaving or growing a thin film are controlled ways to disturb the coupled system, as the process breaks the symmetry and allows continues tuning of stoichiometry. Hence, exploration of surface phenomena offer the opportunity to study how structural, electronic, and magnetic properties react to the broken symmetry. For instance, Freeland, et al., recently reported that the surface of crystalline $La_{2-2x}Sr_{1+2x}Mn_2O_7$ is a nonmagnetic insulator despite the bulk compound being a ferromagnetic metal.[4] As a second example, uncompensated surface charges due to the broken symmetry result in nonlocal depolarization fields that suppress the polarization. To stabilize the ferroelectric phase, a balance between bulk thermodynamics and the screening mechanisms for polarization is needed, which may include oxygen vacancy formation or chemisorption of charge species from the environment.[5] Controllable surface tuning can be accomplished either by manipulating the chemical environment or physically, for example through mechanical stress.

The extreme sensitivity of material properties to external stimuli makes in situ characterization a requirement for understanding and controlled tuning of complex correlated materials. Scanning probe microscopy and spectroscopy (STM, STS) are powerful tools to investigate the electronic properties of the complex correlated oxides and their spatial distribution. STM and STS have been highly successful in real-space maps of electronic inhomogeneity and phase separation in cleavable layered transition metal oxides (TMOs) and other spe-cial cases.[6–9] However, for non-layered TMOs the classical surface science strategies based on repeated sputtering and annealing cycles are unapplicable. Hence, studying the localized behavior with atomic resolution necessitates epitaxial growth of films in situ. This approach allows for other modalities of surface studies including low-energy electron-diffraction intensity vs voltage (LEED I-V)[10,11] and X-ray techniques,[12,13] to name a few. Pulsed-laser deposition (PLD) is one of the most popular growth techniques in condensed matter physics because of its versatility and the relatively easy ability to control certain functionalities by varying growth parameters.[14–24] Compared to other growth methods, PLD has demonstrated a unique capability to obtain high-quality thin films of a wide variety of materials, especially complex oxides which must be grown in an oxygen environment.

Here, we review some recent works based on in situ observations of physical and chemical phenomena on the surfaces of strongly correlated oxides, including atomic-level control of structure and stoichiometry of surfaces, and controllable surface tuning of the property of single crystals. Important aspects of the controlled growth of the oxide films by pulsed-laser deposition are reviewed; the stability of the surface and the polarization against the environment and surface

Dr. Z. Gai, Dr. S. V. Kalinin, Dr. A.-P. Li,
Dr. A. P. Baddorf
Center for Nanophase Materials Sciences
Oak Ridge National Laboratory
Oak Ridge, TN 37830, USA
E-mail: gaiz@ornl.gov
Prof. J. Shen
State Key Laboratory of Surface Physics and Department of Physics
Fudan University
Shanghai 200433, China

DOI: 10.1002/adfm.201203425

chemistry at different temperature are discussed; also mentioned is the direct observation of doped holes and their correlation to the magnetic and transport behaviors of manganites. Controllable surface tuning is demonstrated through chemical environment or local or global stresses. Water, oxygen and external strain are shown to define both structure and properties of oxide interfaces and can be employed as a means to control static and dynamic distributions of electrons and atoms.

2. Atomic-Level Control and Structure of Surface of Strongly Correlated Oxide Thin Films

Pulsed-laser deposition (PLD) is one of the most popular growth techniques in condensed matter physics because of its versatility and the capacity to control materials functionalities by varying growth parameters.[14–24] Compared to other growth methods, PLD has a unique capability to obtain high-quality thin films of a broad range of materials.[20,25,26] The process of PLD involves focusing an intense laser pulse on a flat target, and removing target materials as volatile phases of gases or plasma. Subsequent deposition on the evaporated material on the substrate yield the film of desired material. The distinct advantages of PLD include its simplicity of use and the ability to preserve the stoichiometry of compound materials under optimum conditions. This has made PLD the technique of choice for growing complex materials such as high-Tc superconductor thin films[27] and strongly correlated oxides.[20,22–25,28] However, the atomic-level control of a surface of a strongly correlated oxide thin films is far from simple. A few important aspects of the controlled growth of oxides film with a goal of high quality surfaces are reviewed in this section.

The PLD growth process involves multiple complex steps such as ablation of target material, plasma generation and propagation through vacuum or background gas, deposition of ablated atoms on substrate, non-equilibrium processes on the surface such as diffusion, desorption, nucleation and attachment onto existing atomic steps.[29–32] The resulting PLD film growth mode depends strongly on all of these processes, in addition to the consideration of the cohesive energy between the ablated atoms and the binding energy between the atoms and substrate.[33] Second, the vast majority of studies of oxide films disregard the surface chemistry effects induced by exposure to atmosphere, implicitly postulating kinetic stability of the film. Practically however, the contamination can reduce the stability of the surface, leading to decomposition and desorption of the thin film components at relatively low temperatures in vacuum.[34] Third, reconstruction attributed to surface strain can result in an intrinsic dipole moment even when the bulk is unpolarized for cubic perovskites, as a result, the surface structure can influence polarization stability in an ultrathin film.[35] Furthermore, the magnetic and transport behaviors of manganites are critically related to the spatial distribution and correlation of doped holes. The direct observation of doped holes and their correlation is required to understand the microscopic origins of the exotic properties of hole doped manganites.[28]

Zheng Gai is a research scientist at Oak Ridge National Laboratory, USA and an adjunct professor with Department of Material Science and Engineering, University of Tennessee, Knoxville. She received her B.Sc (1989) and Ph.D (1995) from Peking University, Beijing, China. Her research interests include growth, imaging, magnetic and electronic property characterizations of thin film of complex oxides, functional nanostructures and devices.

2.1. Growth Diagram of $La_{0.7}Sr_{0.3}MnO_3$ Thin Films

The PLD growth process involves multiple complex steps with cross-linked parameters. The background gas pressure plays an important role in plume collisions while acting to compensate film stoichiometry;[14] deposition rate controls the supersaturation value to influence the critical nucleus and density of nucleation sites;[14,30] the substrate temperature has a critical influence on the diffusion barrier which may strongly affect the growth mode. Although various kinds of growth modes have been observed for oxide thin films under different growth conditions,[36–38] growth diagrams which combines multiple parameters and produces a complete picture is still lacking.

The broad variety of the growth modes of $La_{0.7}Sr_{0.3}MnO_3$ thin films on $SrTiO_3$ substrates using pulsed laser deposition were explored by tuning growth temperature, pressure and laser fluence.[33] Different thin film morphology, crystallinity and stoichiometry have been observed depending on growth parameters. To understand the microscopic origin of the adatom nucleation, step advance processes, and their relationship to film growth, a growth diagram was constructed by combining the theoretical treatment in Ref. [32] on the PLD growth of oxide thin films and the film stoichiometry which is described using the supersaturation of the corresponding vapor to solid process in **Figure 1**. Three boundaries between highly and poorly crystallized growth, layer-by-layer and 3D growth, stoichiometric and non-stoichiometric growth were quantitatively identified in the growth diagram. Experimental results and the theoretical model were compared to test the feasibility of the growth diagram.

The temperature dependence of the nucleation process defines the phase boundary of the crystallinity of thin films. During PLD growth, the laser ablation generates a large atomic flux. These incoming atoms become adatoms on the substrate surface and subsequently diffuse in the surface plane. Some coalesce and become nuclei of the new islands. When the sample temperature is low, the nucleation rate is low since thermal energy is small compared to the the nucleation barrier. At the same time, the atom exchange rate between gas and

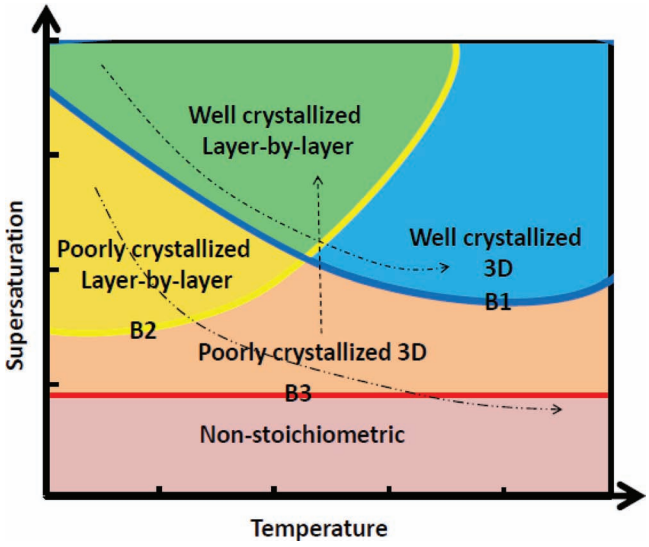

Figure 1. Qualitative comparison between experimental results and theoretical growth diagram. The theoretically constructed growth diagram. B1 (blue): boundary between the poorly crystallized and well crystallized growth. B2 (yellow): boundary between layer-by-layer and 3D growth. B3 (red): boundary between stoichiometric and non-stoichiometric growth. Arrows description: dash-dot-dot: temperature increase (720 °C, 776 °C, 840 °C) under constant laser fluence (1J/cm^2) and pressure; dash-dot: temperature increase (660 °C, 760 °C) under constant laser fluence (4J/cm^2) and pressure; long dash: laser fluence increase (1J/cm^2, 2.2 J/cm^2) under constant temperature and pressure; solid: pressure increase under constant temperature (730 °C) and laser fluence (1J/cm^2).

solid is low. Thus, the films are not well crystallized. When the temperature is high, the nucleation rate is limited due to a high atom exchange rate between gas and solid. However, it is easier to overcome the nucleation energy barrier to form nuclei and hence the films are well crystallized. Consequently, there is a boundary (blue B1 boundary in Figure 1) that divides the poorly crystallized and well crystallized growth modes.

The competition between nucleation and step advance (the growth of 2D islands and advance of steps) determines the boundary (yellow B2 boundary in Figure 1) of layer-by-layer and 3D growth. Besides nucleation, another way for adatoms to contribute to the film growth is to attach to existing nuclei or steps causing step advance. The process includes the surface diffusion of adatoms towards the steps or edges of nuclei and incorporation of the adatoms into the kinks. It is worth to mention that the processes at the early stage of a monolayer deposition such as nucleation and surface migration of the adatoms are more important to determine the growth properties.[2] In such case, the competition between the nucleation rate and the step advance rate becomes a crucial factor to determine the growth mode. If the nucleation rate is much higher than the rate of step advance, new nuclei can form on top of existing islands before the completion of the underlying layer. In turn, several layers can grow simultaneously, causing 3D growth. If the nucleation rate is much lower than the rate of step advance, new nuclei will form after most of the underlying layer is filled, which gives rise to a layer-by-layer growth mode.

The boundary B3 (red online in Figure 1) corresponds to $\Delta\mu = 0$. Supersaturation $\Delta\mu$ is the chemical potential difference of adatoms transitioning from their quasi-vapor phase (the mobile adatoms on the surface and the background oxygen in the gas phase) near the substrate to their solid phase on the substrate. Below B3 the growth is non-stoichiometric due to the inability of completing the thermo-chemical transition from the quasi-vapor phase to the solid phase of the intended compound.[39] Above B3 the film can be grown with the right stoichiometry.

A good fit of the experimental observation with the growth diagram was found. The experimental AFM images for different growth conditions fit into the theoretical growth diagram. As a guide, different arrows are used to illustrate the qualitative dependence of the growth mode under different growth parameters in Figure 1. Supersaturation plays an important role in constructing and understanding growth diagrams for PLD thin film growth of complex oxides. This case study demonstrates that a more comprehensive understanding and prediction of the growth mode using PLD is possible.

The experimental and theoretical results in this work are consistent with the findings of Metev et al.[14,40] in which a high deposition rate (high supersaturation) and a low growth temperature favored a 2D growth mode. The dependence of the boundary between step-flow growth and 2D island formation constructed by Hong et al.[36] on the atomic flux (supersaturation) differ from the findings of this work. On the other hand, the boundary constructed by Hong et al.[36] has not been verified by experiments. The observation of Ohtomo and Hwang[37] also fits nicely in this more complete growth diagram because according to the theoretical model, the supersaturation decreases with temperature and increases with oxygen pressure.

2.2. Surface Stability of Epitaxial $SrRuO_3$ Films

Perovskite $SrRuO_3$ films have attracted application for oxide thin film research due to their outstanding electrical and magnetic properties. $SrRuO_3$ is also a promising electrode material for oxide electronic devices such as ferroelectric heterostructures and non-volatile ferroelectric random access memories (FeRAM), due to its high conductivity and low lattice misfit with many functional perovskite transition metal oxides.[41–43] $SrRuO_3$ surfaces appear to be chemically inert and are one of the few conducting crystalline surfaces to produce an unchanged low energy electron diffraction pattern after exposure to atmosphere (comparable in this way to gold). In reality, careful surface sensitive probes, including scanning tunneling microscopy (STM), X-ray photoemission and high resolution electron energy loss spectroscopies (XPS and HREELS), thermal desorption spectroscopy (TDS), and low energy and reflection high energy electron diffraction (LEED and RHEED) reveal that exposure to atmosphere, even for short times, leads to hydrocarbon contamination of the $SrRuO_3$ surface.[34] This contamination reduces the stability of the surface, leading to decomposition and desorption of the thin film components at relatively low temperatures in vacuum.

Heteroepitaxial $SrRuO_3$ thin films (thickness: 4–10 nm) were grown on TiO_2-terminated $SrTiO_3$ (001) substrates by pulsed laser deposition as described previously. This procedure

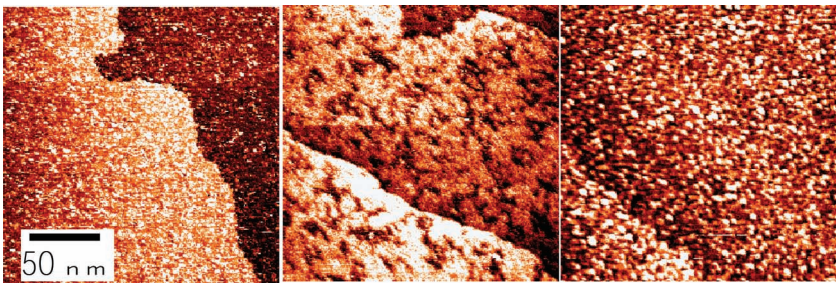

Figure 2. STM images of $SrRuO_3$ films after growth and transfer through air, as grown (left), after annealing to 300 °C (middle), and after annealing to 500 °C (right). Anneals were performed in high vacuum and images recorded at room temperature. Adapted with permission.[34] Copyright 2005, Elsevier.

produces an atomically flat surface with single unit cell steps. After reinsertion into high vacuum (≈10^{-9} Torr), a (1 × 1) LEED pattern was observed confirming a well-ordered surface structure, however patterns irreversibly disappeared after annealing for 10 minutes in vacuum at temperatures as low as ≈100–200 °C, well below the 700 °C temperature at which they were grown.

Evolution of the surface morphology due to annealing was studied by scanning tunneling microscopy (STM). The surface of air-exposed $SrRuO_3$ exhibits unit cell steps; at the same time, large number of irregularly shaped white particles can be observed on the terraces (**Figure 2** left). Based on high resolution electron energy loss spectroscopy (HREELS) data, the particles can be identified as hydrocarbon contaminates. These hydrocarbons are a destabilizing force, reducing the surface at relatively low temperatures ≈300 °C in vacuum (Figure 2 middle). This leads to a decomposition of the surface layer accompanied by desorption of SrO and metallic Ru and the formation of one or two layer deep pits. At higher temperatures, above 500 °C, the remaining surface material forms nanoparticles of Sr-rich ruthenates and metallic Ru (Figure 2 right). After annealing as high as ≈700 °C, atomic steps can still be observed, which provides evidence that only a few layers of $SrRuO_3$ have decomposed and contribute to the spherical particles, while the bulk of the material is stable.

Stable $SrRuO_3$ surfaces, which retain diffraction patterns above 600 °C, can be formed by avoiding exposure to atmosphere, i.e., by working with in situ prepared surfaces. Surfaces exposed to air can also be stabilized by burning off hydrocarbons through annealing the films in high oxygen pressures. Overall, while vast majority of studies of oxide films disregard the effects of surface chemistry and exposure to atmosphere on surface functionalities, these studies demonstate that these effects ar significant even for such inert oxides as $SrRuO_3$.

2.3. Polar Distortion in Ultrathin $BaTiO_3$ Films Studied by In Situ LEED *I–V*

In ferroelectric materials, discontinuity of the normal component of polarization results in a polarization charge and associated depolarization electric field,[44] destabilizing the ferroelectric phase in ultra-thin layers. The stability of the ferroelectric state ultimately is determined by the efficiency of screening. Remarkably, the minimum ferroelectric film thickness observed has dropped from approximately tens of micrometers in the 1950s to several unit cells recently, reflecting advances in both theory and materials synthesis and characterization. First principles theory has predicted polarization in $BaTiO_3$ films as thin as six unit cells[45] or further reduced to three unit cells by polarization in adjacent electrodes.[46] However, fabrication of films free of pinholes over macroscopic length scales required for capacitor fabrication, as well as in situ fabrication of top electrodes to avoid chemisorption represents technological complications that can preclude direct measurements in ultrathin films.

The structure, and consequently the polarization, of ultrathin films can be determined by low energy electron diffraction intensity vs voltage (LEED-IV). This approach bypasses the problems of pinholes as diffraction peaks sample only the ideal (crystalline) regions. Fully strained epitaxial $BaTiO_3/SrRuO_3$ bilayers were grown on (001)-oriented TiO_2-terminated $SrTiO_3$ substrates using a KrF excimer laser with layer thickness monitored by high-pressure reflection high-energy electron diffraction (RHEED).[35] Samples were then transferred to a LEED system without exposure to air. Experimental LEED-IV data was acquired and modeled for 4 ML and 10 ML $BaTiO_3$ films (**Figure 3**). 11 and 8 symmetrically distinct beams were determined, respectively. Modeling of intensities using multiple scattering electron codes ruled out a symmetric non-polar unit cell. Instead, the best fits for both film thicknesses indicates an outward displacement of Ti and Ba and inward displacement of O relative to the unit cell center, corresponding to an upward polarization. These displacements are minimal in the outermost BaO layer, but similar to those seen in bulk $BaTiO_3$ away from the surface.

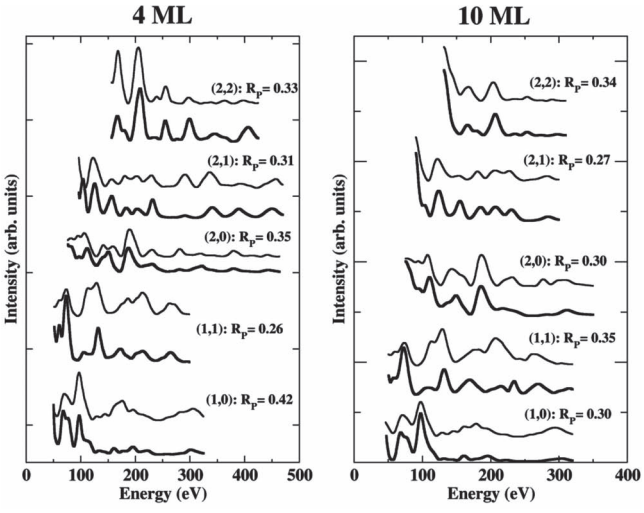

Figure 3. Comparison between several LEED-IV experimental measurements (thick) and calculated intensities (thin) for the best-fit structure found for the 4 ML and 10 ML $BaTiO_3$ films. Adapted with permission.[35] Copyright 2008, The American Physical Society.

Polarization in $BaTiO_3$ at 4 ML is below the critical thickness predicted by Junquera and Ghosez.[47] It is likely that the polar state in these ultra-thin films is determined by intrinsic electrostatic boundary conditions at the surfaces. This explains the observation of a uniform singly oriented domain. It is likely, then, that the film is polarized but not ferroelectric, that is unable to be switched to the reverse polarization. The reduced polarization measured at the surface can also be attributed to the energetics of the surface relaxation, which oppose an upward polarization.[48] In general, we observe that surface structure will be even more influential as studies explore thinner films and controlled environments with in situ characterization by surface sensitive techniques will be vital.

2.4. Visualization of Local Holes with Atomic Resolution

The fascinating trans-port properties in perovskite manganites depend sensitively on the hole doping level as well as ionic sizes of elements.[49–51] The polaron effect due to strong electron-lattice coupling[52–55] is central to understanding the intriguing transport prop-erties of the colossal magnetoresistance (CMR) manganites. Experimentally, research based on scattering studies in reciprocal space has demon-strated that complex effects such as polaron corre-lation, ordering, and charge localization are critically involved in the metal-insulator transition and intrinsic phase separation. However, the forma-tion of small polarons by doped holes requires investigation with real-space imag-ing tools to understand the microscopic origins of the exotic properties of hole-doped manganites. Scanning tunneling microscopy (STM) and spectroscopy have been highly successful in real-space studying electronic inhomogeneity and phase separation in cleavable layered transition metal oxides (TMOs) and certain spe-cial cases.[6–9] However, for non-layered TMOs, there is no doubt that epitaxial growth of manganite thin films offers the most reliable and universal means to study the doped holes with atomic resolution using in situ STM. Epitaxially grown $(La_{5/8-x}Pr_x)Ca_{3/8}MnO_3$, $\times = 0.3$, thin films (LPCMO) were used as a prototype system to study the real-space distribution of the doped holes by means of in situ STM in ultrahigh vacuum (base pressure $<1 \times 10^{-10}$ torr).[28]

With the STM operated in the dual bias mode, localized holes in the Mn-O surface layer can be imaged directly with atomic resolution. A regular square lattice oriented along <100> directions is clearly visible in both occupied and unoccupied state images obtained simultaneously in the same area, as shown in **Figure 4**a,b. The line profiles taken from the same location of the occupied-state (red) and unoccupied-state (black) images in Figure 4c, illustrate that there are two types of lattice sites with different height contrast. The bright sites in the unoccupied-state image become dark sites in the occupied-state image, which is a strong indica-tion that the contrast has an electronic origin. The height difference between the bright and dark sites is particularly large in the unoccupied-state image, which is about 1.0 Å as com-pared with 0.3 Å in the occupied-state image. In the unoccupied-state image, the brighter sites should cor-respond to the locations of the Mn^{4+} ions (localized holes), which have a high-density unoccupied e_g state just above Fermi level that gives rise to a relatively larger tunneling current. The contrast between the Mn^{3+} and the Mn^{4+} sites is reversed and becomes weaker in the occupied-state image, since Mn^{3+} has four (three t_{2g} and one e_g) electrons and Mn^{4+} has three (t_{2g}) electrons below the Fermi level that can contribute to the tunneling current under the experimental bias voltage.

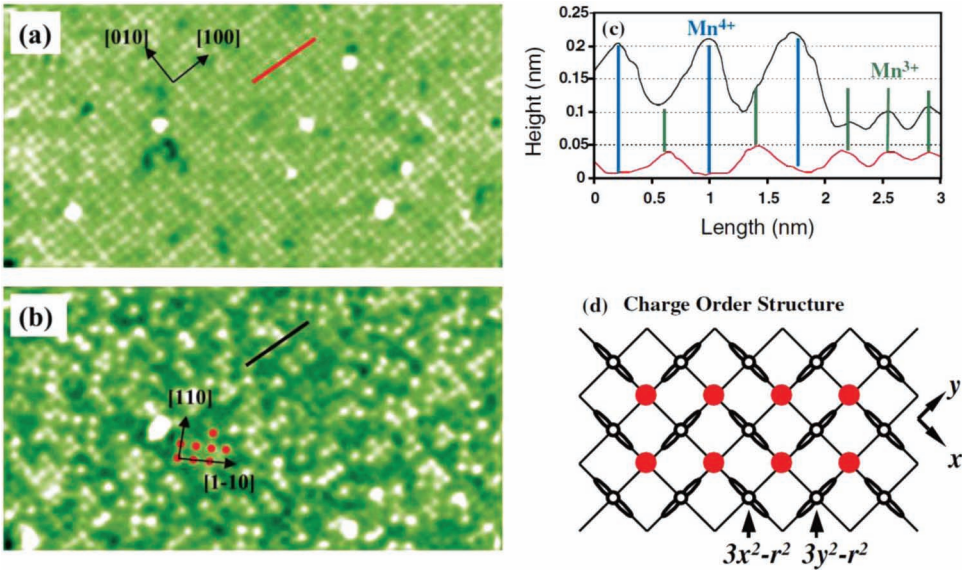

Figure 4. 20 nm × 10 nm dual bias STM images obtained simultaneously in the same area for the paramagnetic state of a 120 nm LPCMO film. a) Occupied-state image and b) unoccupied-state image. In the unoccupied-state image, the brighter and darker lattice sites correspond to Mn^{4+} (localized hole) and Mn^{3+} ions, respectively. The relative contrast between Mn^{4+} and Mn^{3+} ions is reversed in the occupied-state image. c) Marked line profiles showing the relative contrast between Mn^{4+} (indicated by blue lines) and Mn^{3+} (indicated by green lines) ions. The CE-type CO cluster is indicated by the red spots in the unoccupied-state image, with a schematic picture shown in (d). Adapted with permission.[28] Copyright 2005, The American Physical Society.

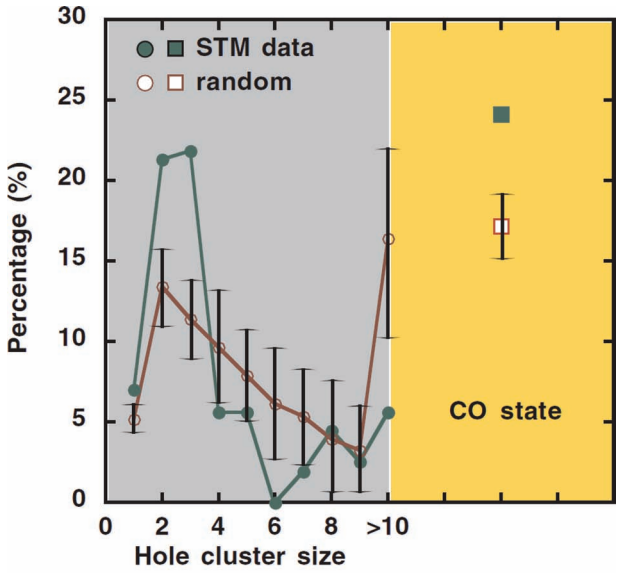

Figure 5. Distribution of holes forming the non-CO (left panel) and CO (right panel) clusters (normalized by total number of holes) obtained from Figure 4b, which is compared with that of a 2DRD with the same doping level. The error bars represent the standard deviations for the random distribution when using the same number of holes from the experimental data. Adapted with permission.[28] Copyright 2005, The American Physical Society.

In contrast to a random distribution, these doped holes show strong short-range correlation and clear pref-erence of forming nanoscale CE-type charge-order-like clusters, which Mn^{3+} and Mn^{4+} ions are alternately arranged in a checkerboard pattern. **Figure 5** shows the statistical distribution of the non-CO and CO clusters obtained from Figure 4b, which is compared with that of a two-dimensional ran-dom distribution (2DRD) with the same doping level. Those holes occupying neighboring sites along the [110] and/or [1-10] directions are viewed as CE-type CO clusters as indicated (red dots) in Figure 4b and those along the [100] and/or [010] directions are viewed as non-CO the doped holes. The results provide insights of the nature of the electronic phase separation in the LPCMO compound.

3. Controllable Surface Tuning of the Properties of Strongly Correlated Oxides

3.1. Chemical Screening of Ferroelectric Surfaces: An In Situ Study Ultra-Thin $BaTiO_3$ Films Exposed to H_2O

As ferroelectric materials are made thinner, their properties are even more sensitive to the state of the surface than non-polarized materials due to the accumulation of surface charge and mechanisms for screening. Uncompensated surface charges due to the discontinuity of the normal polarization component result in non-local depolarization fields that suppress the polarization. Several reports show strong experimental evidence for surface compensation by ionic adsorption for relatively thick ferroelectric films exposed to an ambient environment.[56–59] Wang et al.[5] reported that the reversible adsorption of oxygen, which is associated with the charge transfer on the surface of ultrathin $PbTiO_3$ film (O2- in the lattice and neutral O_2 in the gas phase), and results in reversible polarization switching between two polar states. Traditional surface science methods generally suggest that defect free perovskite surfaces are stable with respect to water adsorption for small exposures,[10] but being polar, water could significantly screen surface charges.

We examined the stability and structure of 10 ML thick $BaTiO_3$ films in ultrahigh vacuum after controlled exposure to H_2O as determined by in situ low energy electron diffraction intensity vs. voltage (LEED I–V) analysis.[60] Ultrathin 10 ML $BaTiO_3$ films were grown on $SrRuO_3/SrTiO_3$ by pulsed laser deposition (PLD) under growth conditions reported elsewhere.[25,43] Surface structures before and after exposure to water were determined using low energy electron diffraction intensity vs. voltage (LEED-IV). Exposures up to 104 L of water led to little structural change. However exposures about 10 times greater modified the diffraction intensities. For reference, this exposure corresponds to exposure to ambient air for less than a tenth of a second.

In combination with density functional theory (DFT) calculations, the best interpretation of the data suggests a partial monolayer of OH from dissociated water. The relatively large exposures needed follow from the low probability for water dissociation. In DFT calculations, molecular water is found to adsorb on BaO terminated surfaces with the oxygen atom down, and bonded to the surface cation. The presence of polar OH molecules at the surface significantly modifies the surface charge induced by polarization. The effect is sufficiently strong, with the energy contributions from chemical bonds trumping that of the polarization, that LEED-IV structural measurements show the polarization direction in the film is flipped by adsorption.

These findings reconcile the existing knowledge of ferroelectric stability in ambient environments and existing surface science results. Ultrathin ferroelectric $BaTiO_3$ films, where interfacial effects can dominate the physics of the film interior, show complete polarization inversion by water vapor exposures while thicker films may only be affected near the surface. Furthermore, these studies suggest that maintaining chemical integrity of $BaTiO_3$ is possible only if material handling is performed in a dry atmosphere.

3.2. An Oxygen-Induced Surface Reconstruction of $SrRuO_3$ and its Effect on the $BaTiO_3$ Interface

Advances in atomically-controlled oxide growth have generated new classes of materials with physical properties highly dependent on abrupt interfaces.[16,47,61–64] At interfaces, the sensitivity of oxide properties to electron concentration is coupled to charge transfer, structure, and spin to produce behavior including interface mediated conduction,[65,67] superconductivity,[65] magnetism,[68] and phase transitions[69–70] in parent materials lacking these attributes. The response of oxides to structural instabilities or disorder is naturally greater in two-dimensional systems, as evidenced by Anderson localization, Peierls instability or charge

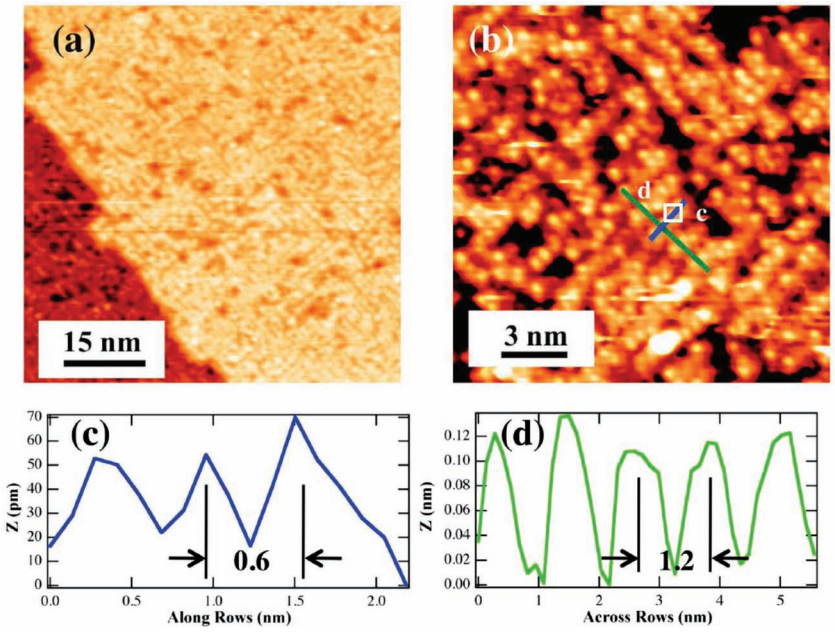

Figure 6. In situ STM images of a $SrRuO_3$ film illustrating a) the rows and b) at higher resolution with height cross-sections c) along and d) across the rows. A period doubling between the rows is observed. Adapted with permission.[75] Copyright 2010, American Chemical Society.

density wave transitions. Oxygen stoichiometry plays a central role in defining both structure and properties of oxide interfaces.[71–73] Unfortunately, few atomic scale studies of interface structures exist for complex oxides, due to a need for multiple tools to probe subsurface features, the need for a highly controlled environment,[34,74] and the insulating nature of many oxides.

By combining a number of structural techniques, both in situ and ex situ, we have followed the growth of ferroelectric $BaTiO_3$ on an $SrRuO_3$ electrode on a $SrTiO_3$ substrate. Films of 1, 2, 4, and 10 unit cells of $BaTiO_3$ were grown on $SrRuO_3/SrTiO_3$ as detailed elsewhere.[75] The growth quality and quantity of deposited material were confirmed using Reflection High Energy Electron Diffraction (RHEED) during deposition. The expectation, based on ex situ atomic force microscopy (AFM) studies of $SrRuO_3$ films, was that the interface between $SrRuO_3$ and $BaTiO_3$ would be atomically flat. Instead, high resolution scanning tunneling microscopy (STM) images of the $SrRuO_3$ surface taken without exposure to air revealed a more complex picture. STM images, such as those shown in **Figures 6**a,b, resolve features with the size of an individual unit cell (0.4 nm). These images show rows of atoms in the surface plane oriented along <110> and <1-10> crystallographic directions. These rows are interspersed with a number of missing atoms, creating a large fraction of defects in the ordering. A line height analysis (Figure 6c) reveals the spacing along the rows corresponds to a single unit cell ($\sqrt{2}$ times the lattice constant of $SrTiO_3$, 0.391 nm), while the spacing between rows is twice that value. It is clear that these rows and holes, unobserved with ex situ AFM, will provide a profound effect on the surface and interface properties and on subsequent growth mechanisms of materials such as $BaTiO_3$. We explored the structure observed using density functional theory (DFT) models. These found that restructuring of SrO dimers that preserve charge neutrality was much more likely than that of rearranging individual atoms. The suggested model is that of SrO dimers removed from and elevated onto the surface layer to form rows as shown in **Figure 7**.

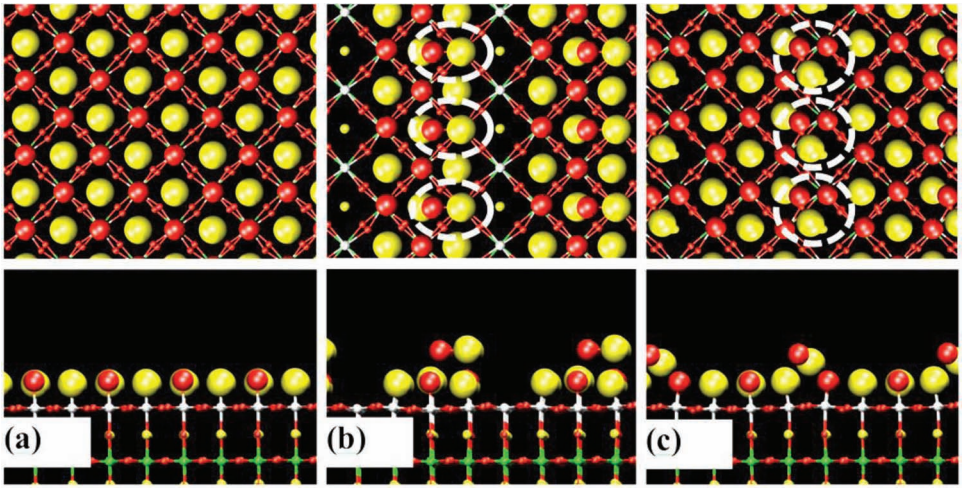

Figure 7. $SrRuO_3$ surface models developed from DFT modeling viewed from the top (upper panels) and side (lower panels). a) The bulk terminated, flat surface model. b) The minimum energy configuration when one row of SrO is "elevated" on top of the surface. c) Addition of one O (in red) per unit cell, which energetically prefers the site vacated by the Sr, increases the stability substantially. Adapted with permission.[75] Copyright 2010, American Chemical Society.

To examine the structure of the buried $BaTiO_3/SrRuO_3$ interface, we employed low energy electron diffraction (LEED). Patterns were obtained from $SrRuO_3$ and from thin films of $BaTiO_3$ on $SrRuO_3$. The diffraction pattern from $SrRuO_3$ thin film surfaces had not only the square pattern expected from a bulk-terminated film, but also an additional spot halfway between each bulk spot. This pattern showed the surface unit cell periodicity was doubled consistent with the rows (in two domains) observed in STM that were separated by twice the bulk lattice constant. As 1–2 layers of $BaTiO_3$ were grown on $SrRuO_3$, the additional LEED spots remained, however the relative intensities of diffraction spots were altered from those observed from $SrRuO_3$ alone. This change in relative intensities indicates a change of structure, with two important implications. First, this pattern must represent the order of the $BaTiO_3$ film, and cannot arise solely from exposed remnants of $SrRuO_3$. Second, this shows that the $SrRuO_3$ reconstruction influences the structure of the $BaTiO_3$ at the interface, which does not share the symmetry of bulk $BaTiO_3$, but instead has a periodicity two times larger in the plane of the interface. Growth of thicker $BaTiO_3$ films reverts the observed LEED pattern to the symmetry of the bulk crystal. In this regime, the LEED electrons cannot penetrate to the interface and instead sample the outermost region of the $BaTiO_3$ alone.

The structural change at the buried interface is supported by cross-sectional z-contrast scanning transmission electron microscopy (STEM). **Figure 8** clearly shows the interface between $SrRuO_3$ and $BaTiO_3$ where TiO_2 planes take over from more intense RuO_2 planes. Image intensity profiles shown in Figure 8c reveal that the interface is not as uniform as the image alone might imply. The first BaO column marked Ba* has a considerably reduced intensity relative to others. This suggests the depletion of Ba or presence of Sr in this column. A profile from individual rows across the image and track the intensities of the SrO and BaO columns closest to the interface, makes clear that the compositional change is not uniform, and is instead consistent with a structurally reconstructed interface.

3.3. Tunable Metalicity at $La_{5/8}Ca_{3/8}MnO_3$(001) Surface by Oxygen Overlayer

The strong coupling between structural, electronic and magnetic properties is readily apparent in several perovskite manganites.[50] The emerging surface electronic phases can be modified by surface reconstructions which occur due to bond breaking at the surface. The surface structure of epitaxially PLD grown $La_{5/8}Ca_{3/8}MnO_3$ (LCMO) thin films was studied using in situ scanning tunneling microscopy (STM). Atomically resolved STM images reveal that a reconstructed surface and a (1×1) surface can be converted back and forth through adsorption and desorption of oxygen at the surface.[76] Electrical properties of the surfaces are investigated by scanning tunneling spectroscopy (STS). *I–V* curves clearly show that the presence of an oxygen overlayer renders the surface insulating while the (1×1) surface without the oxygen overlayer is metallic.

The surface structure of LCMO films depends strongly on the length of time of post annealing in oxygen. The (1×1) structure (**Figure 9**a) and the $(\sqrt{2} \times \sqrt{2})R45^\circ$ (Figure 9d) structure can be converted back and forth through controlled adsorption and desorption of oxygen at the surface. As indicated by the green arrows in Figure 9, with increasing annealing time in oxygen at 820 K, $(\sqrt{2} \times \sqrt{2})R45^\circ$ patches appear and spread on the otherwise (1×1) surface. Over time, these patches grow until the surface has a nearly complete $(\sqrt{2} \times \sqrt{2})R45^\circ$ structure. It is then possible to return the surface to its (1×1)

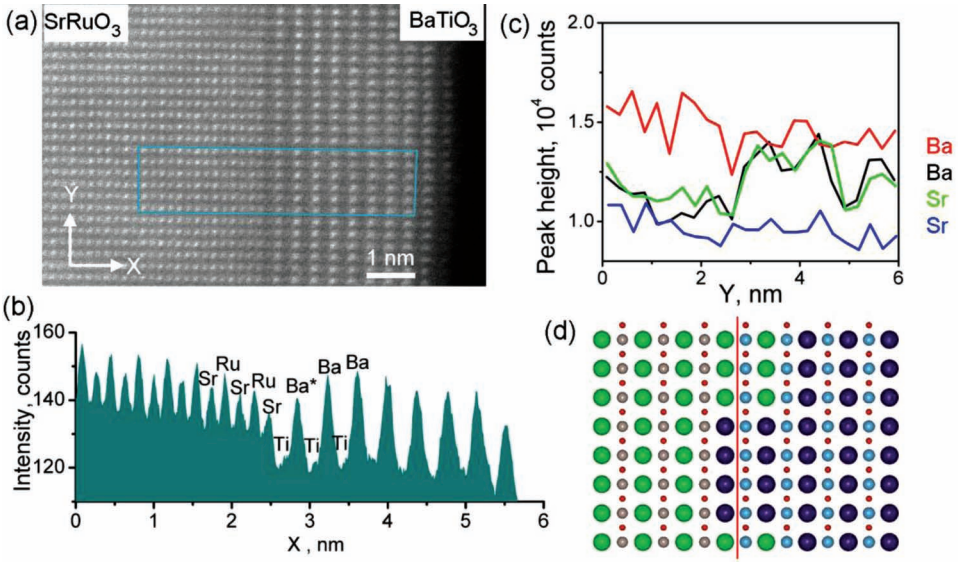

Figure 8. a) High angle annular dark field STEM image of the $BaTiO_3/SrRuO_3/SrTiO_3$ film in cross-section; b) intensity profile averaged over area in the blue box in (a), showing decreased intensity in the first Ba column denoted as Ba*. c) Ba and Sr column intensities in the vicinity of the interface (color coding on right) as a function of vertical coordinate of the image (black Ba and green Sr are corresponding to the first columns near the interface). d) interface structure suggested from STEM images, with ideal interface position indicated by red line (Sr–green, Ru–grey, O- red, Ba–purple, Ti–blue). Adapted with permission.[75] Copyright 2010, American Chemical Society.

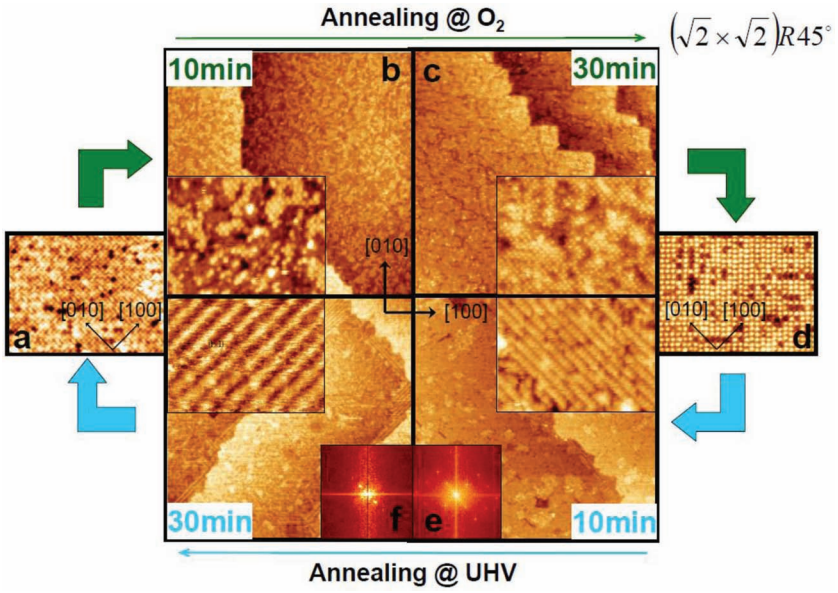

Figure 9. Flowchart of the structural evolution between (1 × 1) and $(\sqrt{2}\times\sqrt{2})R45^\circ$. Arrows indicate the conversion from annealing in oxygen (green) or UHV (blue) respectively. a) Annealing the sample with (1 × 1) structure in oxygen at 820 K for b) 10 min and c) 30 min leads to more $(\sqrt{2}\times\sqrt{2})R45^\circ$ regions coexisting with the (1 × 1) structure, and finally a full $(\sqrt{2}\times\sqrt{2})R45^\circ$ structure d) forms. Annealing the initially $(\sqrt{2}\times\sqrt{2})R45^\circ$ structure (d) in UHV at 680 K for e) 10 min and f) 30 min, $(\sqrt{2}\times2\sqrt{2})R45^\circ$ (insert in (e)) and $(\sqrt{2}\times3\sqrt{2})R45^\circ$ (insert in (f)) patches show up, and finally a full (1 × 1) structure (a) returns. The scan size in (b), (c), (e), and (f) is 150 nm × 150 nm, and in (a), (d) and all the inserts is 16 nm × 12 nm. The fast Fourier Transform (FFT) of the STM images with $(\sqrt{2}\times2\sqrt{2})R45^\circ$ and $(\sqrt{2}\times3\sqrt{2})R45^\circ$ structures are shown as inserts in (e) and (f). Adapted with permission.[76] Copyright 2009, The American Physical Society.

structure by annealing in ultrahigh vacuum at 680 K to remove the oxygen as indicated by the blue arrows in Figure 9. The sequential formation of $(\sqrt{2}\times\sqrt{2})R45^\circ$, $(\sqrt{2}\times2\sqrt{2})R45^\circ$ and $(\sqrt{2}\times3\sqrt{2})R45^\circ$ upon oxygen desorption strongly hints that these surface reconstructions are associated with increasing oxygen deficiency at the surface. By using the STM tip to gently scratch the $(\sqrt{2}\times\sqrt{2})R45^\circ$ surface, the $(\sqrt{2}\times\sqrt{2})R45^\circ$ structure can also be converted to the (1 × 1). A structural model in which the oxygen atoms sit atop every other MnO_6 octahedron and form the $(\sqrt{2}\times\sqrt{2})R45^\circ$ lattice arrangement as shown in the left panel of **Figure 10** was proposed base on the STM observations.

Remarkably, there is a dramatic difference in metalicity for the $(\sqrt{2}\times\sqrt{2})R45^\circ$ structure and the (1 × 1) structure. As clearly indicated by the spectroscopy in Figure 10, right panel, the $(\sqrt{2}\times\sqrt{2})R45^\circ$ surface yields an insulating characteristic with a band gap of about 1.35 eV while the (1 × 1) surface is metallic and shows no band gap.

The insulating behavior of the $(\sqrt{2}\times\sqrt{2})R45^\circ$ surface can be understood based on the bulk phase diagram of the LCMO material (a paramagnetic insulator above T_c). The $(\sqrt{2}\times\sqrt{2})R45^\circ$ surface basically resembles the bulk MnO_6 octahedron structure. Missing the (La,Ca) cations in the $(\sqrt{2}\times\sqrt{2})R45^\circ$ surface may not change the local density of states (DOS) of the MnO_2 layer since the cations do not contribute to bonding and are located far from the Fermi level. Their only contribution is in donating their valence electrons to the Mn and O bands. For the MnO_2 terminated (1 × 1) surface, the $(3^2–r^2)$ orbital is expected to have a lower binding energy than the $(x^2–y^2)$ orbitals due to a lack of Coulomb repulsion from the p_z electron of the missing oxygen at the top of the octahedron.[77] Theoretical calculations of the MnO_2 terminated surface conclude that $(3z^2–r^2)$ is the dominant state for the MnO_2 terminated surface.[78–81] Compared to the $(x^2–y^2)$, the $(3z^2–r^2)$, orbital is more delocalized around the Mn ionic core, leading to more overlapping with the p orbital of the neighboring oxygen atoms. This gives rise to a conductive characteristic along the orbital direction (z normal to the surface).

3.4. Imaging and Strain-Tuning of the Competing Electronic Phases Near the Mott Metal-Insulator Transition in $Sr_3(Ru_{1-x}Mn_x)_2O_7$

The complex interplay between electron and lattice degrees of freedom produces many nearly degenerate electronic states in correlated electron materials. These states determine the functionality of the system, but competition between these states produces highly variable properties whose mechanism remains in debate. By imaging phase domains with electron microscopy and interrogating individual domains in situ via point probe

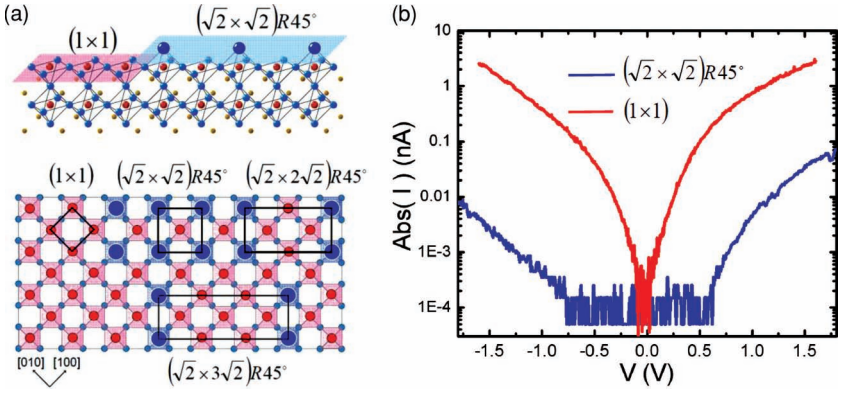

Figure 10. a) Side view (upper panel) and top view (lower panel) of models for the (1 × 1) and $(\sqrt{2}\times\sqrt{2})R45^\circ$ structures, with red, large blue, and small blue balls representing Mn, O atoms located atop MnO_6 octahedron, and O in the MnO_6 layer, respectively. The unit cells of (1 × 1), $(\sqrt{2}\times\sqrt{2})R45^\circ$, $(\sqrt{2}\times2\sqrt{2})R45^\circ$, and $(\sqrt{2}\times3\sqrt{2})R45^\circ$ are outlined in the lower panel. b) STS I/V curves (shown in logarithmic scale) obtained at set points of 1.8 V/ 30 pA and 0.6 V/ 200 pA from the $(\sqrt{2}\times\sqrt{2})R45^\circ$ and the (1 × 1) surfaces, respectively. The (1 × 1) surface shows no bandgap while the $(\sqrt{2}\times\sqrt{2})R45^\circ$ surface shows a 1.35 eV bandgap. Adapted with permission from.[76] Copyright 2009, The American Physical Society.

electron transport spectroscopy in double-layered $Sr_3(Ru_{1-x}Mn_x)_2O_7$ (x = 0 and 0.2), Kim et al.[82] have showed the first real-space evidence that the microscopic phase competition and the Mott-type metal-insulator transition can be tuned by applying a mechanical stress.

Layered $Sr_3Ru_2O_7$ belongs to the Ruddlesden-Popper series with a stacking of two layers of corner- sharing RuO_6 octahedra separated by cation oxide rock-salt layers.[83] The lamellar structure of the ruthenate makes the crystal amenable to creating a fresh *ab* plane by cleaving in situ an ultra-high vacuum (UHV) system. This offers a controlled way to investigate electronic phases using multiple surface analytical techniques. In general, 4d TMOs (e.g., ruthenates) have weaker correlation effects than 3d TMOs (e.g., manganites, cuprates, and cobaltates) as the radial extension of 4d wave functions is significantly larger than that of transition-metal (TM)-3d orbitals.[84] On the other hand, the extended wave functions of the 4d TM enable an interesting competition between local and itinerant physics. Doping the 4d host with a dilute 3d TM is thus extremely effective in tuning valence, spin, and orbital characteristics and, in turn, the macroscopic physical properties as manifested in $Sr_3(Ru_{1-x}$ Mn $_x)_2O_7$.[84,85] In the undoped compound of $Sr_3Ru_2O_7$, a field- induced quantum phase transition was discovered.[86,87] With the substitution of Ru by a few percent of Mn, a metal-to-insulator transition (MIT) and the emergence of a Mott AFM ground state were revealed.[84,85] The MIT is believed to be driven by the onset of AFM correlations with a clear phase boundary between the paramagnetic (PM) metal and AFM insulator regions at $T_c \approx 80$ K for 10% Mn substitution.[84,85]

Single crystals of $Sr_3(Ru_{0.8}Mn_{0.2})_2O_7$ were grown by a floating zone technique.[88] Direct visualization of phase separation was carried out on cleaved single-crystal surfaces in a cryogenic four-probe scanning tunneling microscopy (STM) system.[89] An UHV (pressure $<1.0 \times 10^{-10}$ Torr) field emission scanning electron microscopy (SEM), scanning tunneling spectroscopy (STS), and four-probe STM were used to probe electronic properties on surfaces in situ.[90] The microscopic phase domains were imaged using SEM and the electronic properties of each domain were simultaneously interrogated using the scanning tunneling probes in either spectroscopic or transport modes.

A striking domain contrast is observed with SEM at low temperatures, as shown in **Figure 11**a. Such domain structure disappears at room temperature. Dramatic changes have been observed in the size and location of phase domains in response to thermal cycling. The electronic properties of individual domains are then confirmed by STS measurements. The spatially averaged tunneling *I–V* curve taken in the bright regions is markedly different from that in the dark regions, with a strong suppression of current near E_F in the dark regions (Figure 11b). The derivative of *I–V* data (inset of Figure 11b) reveals an energy gap near E_F in the dark domains, in contrast to a finite density of states in the bright matrix. Thus, the SEM contrast here reflects the electronic state difference between dark and bright regions that correspond to insulating and metallic phases, respectively.

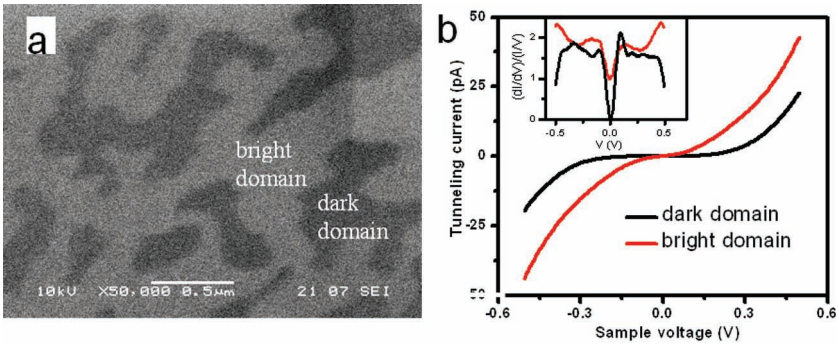

Figure 11. a) Electronic phase domains resolved by cryogenic SEM in the cleaved surfaces of $Sr_3(Ru_{1-x}Mn_x)_2O_7$ At 81 K. b) Averaged tunneling *I–V* curves and derivative conductance (*dI/dV*) curves measured in bright and dark bubble domains. An energy gap is seen in tunneling *I–V* curve of dark domain. The gap is further confirmed by *dI/dV* data, where a differential conductance is essentially zero inside the gap. Adapted with permission.[82] Copyright 2010, National Academy of Sciences, USA.

Based on theoretical simulations, the chemical disorder introduced by the impurity ions of different radii can form large- scale phase separations.[2,91] The inhomogeneity of a chemical origin would occur at the same location in different thermal cycles. On the other hand, pure electronic interactions can also induce inhomogeneity of charge density distribution; however, this inhomogeneity would have a totally random distribution at the nanometer scale.[50,91] Thus, neither electronic interactions nor chemical inhomogeneity can be used to fully explain the above observations. In order to gain insight into the origin of phase separation near the MIT, Kim et al. explored the strain effect on phase domains and percolation by applying mechanical stress.[82] With a piezoelectric sample holder, a uniaxial compressive stress is applied in the ab plane and image the evolution of phase domains are examined in situ. **Figure 12**a,b shows the domain patterns before and after applying strain, respectively. The domain evaluation as a function of stress and time (Figure 12c,d) clearly show that, in the presence of stress, one phase expands dramatically at the expense of the other at a constant temperature. According to theoretical simulation for manganites, the electron-lattice interactions can lead to local energetically favorable configurations and electronic PS over micrometer scales in the presence of strain, induced either externally (stress) or internally (chemical substitution).[92] The real-space images in ruthenates provide the first direct evidence for this scenario. The "gigantic" response of the phase domains to the strain field in $Sr_3(Ru_{0.8}Mn_{0.2})_2O_7$ can stem from the interplay between the spatially confined Mn 3d orbitals and the extended, yet anisotropic, Ru 4d–O 2p electronic backbone of the Ru-O host. Owing to a smaller ionic radius, the Mn substitution for Ru creates an octahedral compression, which alters the relative energies of *d* orbitals and enhances AFM with a possibly orbitally ordered state

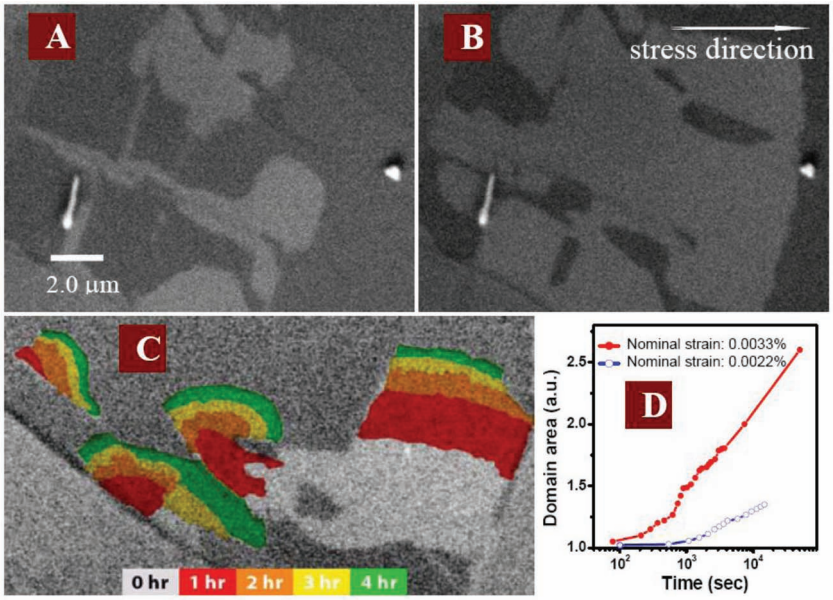

Figure 12. Strain-induced domain evolutions in the cleaved surface of a $Sr_3(Ru_{0.8}Mn_{0.2})_2O_7$. Domain image A) before stress and B) after applying a uniaxial compressive stress in the *ab* plane. C) Domain evolution in time with nominal strain of 0.0022%. D) Domain area change with time. Adapted with permission.[82] Copyright 2010, National Academy of Sciences, USA.

at low *T*. A minute amount of external strain superimposes onto the distortions induced by Mn substitution, thus resulting in a "gigantic" response in insulating domains in $Sr_3(Ru_{0.8}Mn_{0.2})_2O_7$.

A quantitative correlation between the macroscopic metal-insulator transition and the microscopic phase percolation has further been revealed.[82] This work presents the first direct, real-space, observation that a "gigantic" phase domain response to a minute amount of strain can occur in a Mott system. In contrast to the "conventional" way of tuning the Mott transition by chemical doping, it is now demonstrated tuning by strain, paving the way for new control of the electronic properties for electronics and sensing applications. The detailed images of the phase percolation and the dynamic phase competition enable further investigations on the strain control of emergent functionality in correlated electronic materials.

4. Conclusions

This paper reviews several recent in situ observations and tuning of physical and chemical phenomena on the surfaces of strongly correlated oxides, including in situ atomic-level control and structure of surfaces of strongly correlated oxide thin films, and controllable surface tuning of the properties of strongly correlated oxides.

Important aspects of the controlled growth of the oxide films by pulsed-laser deposition were reviewed; the stability of the surface and the polarization against the environment and surface chemistry at different temperatures was explored; also mentioned is the direct observation of doped holes and their correlation to the magnetic and transport behaviors of manganites. This review shows that controllable surface tuning can be either through chemical environment or physically, for example mechanical stress. Water, oxygen, and external strain can define both structure and properties of oxide interfaces and can be employed as a means to control static and dynamic distributions of electrons and atoms.

Acknowledgements

This research was conducted at the Center for Nanophase Materials Sciences, which is sponsored at Oak Ridge National Laboratory by the Scientific User Facilities Division, Office of Basic Energy Sciences, U.S. Department of Energy.

Received: November 21, 2012
Revised: January 10, 2013
Published online: April 5, 2013

[1] C. N. R. Rao, B. Raveau, *Transition Metal Oxides: Structure, Properties, and Synthesis of Ceramic Oxides*, 2nd ed., Wiley–VCH, New York/Weinheim **1998.**
[2] E. Dagotto, *Science* **2005**, *309*, 257.
[3] H. Takagi, H. Y. Hwang, *Science* **2010**, *327*, 1601.
[4] J. W. Freeland, K. E. Gray, L. Ozyuzer, P. Berghuis, E. Badica, J. Kavich, H. Zheng, J. F. Mitchell, *Nat. Mater.* **2004**, *4*, 62.
[5] R. Wang, D. Fong, F. Jiang, M. Highland, P. Fuoss, C. Thompson, A. Kolpak, J. Eastman, S. Streiffer, A. Rappe, G. Stephenson, *Phys. Rev. Lett.* **2009**, *102*, 047601.
[6] C. Renner, G. Aeppli, B.-G. Kim, Y.-A. Soh, S.-W. Cheong, *Nature* **2002**, *416*, 518.
[7] M. Fäth, *Science* **1999**, *285*, 1540.
[8] S. H. Pan, J. P. O'Neal, R. L. Badzey, C. Chamon, H. Ding, J. R. Engelbrecht, Z. Wang, H. Eisaki, S. Uchida, A. K. Gupta, K. W. Ng, E. W. Hudson, K. M. Lang, J. C. Davis, *Nature* **2001**, *413*, 282.
[9] M. Vershinin, S. Misra, S. Ono, Y. Abe, Y. Ando, A. Yazdani, *Science* **2004**, *303*, 1995.
[10] V. E. Henrich, P. A. Cox, *The Surface Science of Metal Oxides*, Cambridge University Press, Cambridge **1994.**
[11] N. Bickel, G. Schmidt, K. Heinz, K. Müller, *Phys. Rev. Lett.* **1989**, *62*, 2009.
[12] S. Streiffer, J. Eastman, D. Fong, C. Thompson, A. Munkholm, M. Ramana Murty, O. Auciello, G. Bai, G. Stephenson, *Phys. Rev. Lett.* **2002**, 89.
[13] D. D. Fong, G. B. Stephenson, S. K. Streiffer, J. A. Eastman, O. Auciello, P. H. Fuoss, C. Thompson, *Science* **2004**, *304*, 1650.
[14] D. B. Chrisey, G. K. Hubler, *Pulse Laser Deposition of Thin Films*; John Wiley & Sons: New York, **1994**.
[15] H. M. Christen, G. Eres, *J. Phys.: Condens. Matter* **2008**, *20*, 264005.
[16] A. Ohtomo, H. Y. Hwang, *Nature* **2004**, *427*, 423.
[17] D. P. Norton, *Mater. Sci. Eng., R* **2004**, *43*, 139.
[18] H. W. Jang, D. A. Felker, C. W. Bark, Y. Wang, M. K. Niranjan, C. T. Nelson, Y. Zhang, D. Su, C. M. Folkman, S. H. Baek,

S. Lee, K. Janicka, Y. Zhu, X. Q. Pan, D. D. Fong, E. Y. Tsymbal, M. S. Rzchowski, C. B. Eom, *Science* **2011**, *331*, 886.
[19] T. J. Jackson, S. B. Palmer, *J. Phys. D: Appl. Phys.* **1994**, *27*, 1581.
[20] M. Dawber, J. F. Scott, *Rev. Mod. Phys.* **2005**, *77*, 1083.
[21] W. Eerenstein, N. D. Mathur, J. F. Scott, *Nature* **2006**, *442*, 759.
[22] J. Wang, J. B. Neaton, H. Zheng, V. Nagarajan, S. B. Ogale, B. Liu, D. Viehland, V. Vaithyanathan, D. G. Schlom, U. V Waghmare, N. a Spaldin, K. M. Rabe, M. Wuttig, R. Ramesh, *Science* **2003**, *299*, 1719.
[23] J. M. Rondinelli, N. A. Spaldin, *Adv. Mater.* **2011**, *23*, 3363.
[24] W. Prellier, M. P. Singh, P. Murugavel, *J. Phys. Condens. Matter* **2005**, *17*, R803.
[25] P. Willmott, J. Huber, *Rev. Mod. Phys.* **2000**, *72*, 315.
[26] J. Shen, Z. Gai, J. Kirschner, *Surf. Sci. Rep.* **2004**, *52*, 163.
[27] D. Dijkkamp, T. Venkatesan, X. D. Wu, S. A. Shaheen, N. Jisrawi, Y. H. Min-Lee, W. L. McLean, M. Croft, *Appl. Phys. Lett.* **1987**, *51*, 619.
[28] J. X. Ma, D. T. Gillaspie, E. W. Plummer, J. Shen, *Phys. Rev. Lett.* **2005**, *95*, 237210.
[29] P. R. Willmott, J. R. Huber, *Rev. Mod. Phys.* **2000**, *72*, 315.
[30] P. R. Willmott, *Prog. Surf. Sci.* **2004**, *76*, 163.
[31] M. N. R. Ashfold, F. Claeyssens, G. M. Fuge, S. J. Henley, *Chem. Soc. Rev.* **2004**, *33*, 23.
[32] I. V Markov, *Crystal Growth for Beginners: Fundamentals of Nucleation, Crystal Growth and Epitaxy*, 2nd ed.,World Scientific, New Jersey **2003**.
[33] H. Guo, D. Sun, W. Wang, Z. Gai, I. Ivan Kravchenko, J. Shao, L. Jiang, T. Z. Ward, P. C. Snijders, L. Yin, J. Shen, X. Xu, arXiv:1210.5989 [cond-mat.mtrl-sci] **2012**.
[34] J. Shin, S. V. V Kalinin, H. N. N. Lee, H. M. M. Christen, R. G. G. Moore, E. W. W. Plummer, a. P. P. Baddorf, *Surface Science* **2005**, *581*, 118.
[35] J. Shin, V. B. Nascimento, a. Y. Borisevich, E. W. Plummer, S. V Kalinin, a. P. Baddorf, *Phys. Rev. B* **2008**, *77*, 245437.
[36] W. Hong, H. N. Lee, M. Yoon, H. M. Christen, D. H. Lowndes, Z. Suo, Z. Zhang, *Phys. Rev. Lett.* **2005**, *95*, 95501.
[37] A. Ohtomo, H. Y. Hwang, *J. Appl. Phys.* **2007**, *102*, 83704.
[38] S. K. Sinha, R. Bhattacharya, S. K. Ray, I. Manna, *Mater. Lett.* **2011**, *65*, 146.
[39] W. Wang, Z. Gai, M. Chi, J. D. Fowlkes, J. Yi, L. Zhu, X. Cheng, D. J. Keavney, P. C. Snijders, T. Z. Ward, J. Shen, X. Xu, *Phys. Rev. B* **2012**, *85*, 155411.
[40] S. Metev, K. Meteva, *Appl. Surf. Sci.* **1989**, *43*, 402.
[41] C. B. Eom, R. J. Cava, R. M. Fleming, J. M. Phillips, R. B. Vandover, J. H. Marshall, J. W. P. Hsu, J. J. Krajewski, W. F. Peck, *Science* **1992**, *258*, 1766.
[42] J. P. Mercurio, J. H. Yi, M. Manier, P. Thomas, *J. Alloys Compd.* **2000**, *308*, 77.
[43] H. N. Lee, D. Hesse, N. Zakharov, U. Gosele, *Science* **2002**, *296*, 2006.
[44] M. E. Lines, A. M. Glass, *Principles and Applications of Ferroelectrics and Related Materials*, Clarendon press, Oxford **1977**.
[45] J. Junquera, M. Zimmer, P. Ordejon, P. Ghosez, *Phys. Rev. B* **2003**, *67*, 155327.
[46] G. Gerra, A. K. Tagantsev, N. Setter, K. Parlinski, *Phys. Rev. Lett.* **2006**, *96*, 107603.
[47] J. Junquera, P. Ghosez, *Nature* **2003**, *422*, 506.
[48] M. Mayr, A. Moreo, J. A. Verges, J. Arispe, A. Feiguin, E. Dagotto, *Phys. Rev. Lett.* **2001**, *86*, 135.
[49] M. Imada, A. Fujimori, Y. Tokura, *Rev. Mod. Phys.* **1998**, *70*, 1039.
[50] E. Dagotto, T. Hotta, A. Moreo, *Phys. Rep.* **2001**, *344*, 1.
[51] M. B. Salamon, M. Jaime, *Rev. Mod. Phys.* **2001**, *73*, 583.
[52] G. Zhao, K. Conder, H. Keller, K. A. Müller, *Nature* **1996**, *381*, 676.
[53] T. Egami, D. Louca, *Phys. Rev. B* **2002**, *65*, 094422.
[54] H. Röder, J. Zang, A. Bishop, *Phys. Rev. Lett.* **1996**, *76*, 1356.
[55] A. Millis, P. Littlewood, B. Shraiman, *Phys. Rev. Lett.* **1995**, *74*, 5144.
[56] S. V Kalinin, D. A. Bonnell, *Phys. Rev. B* **2001**, *63*, 125411.
[57] T. Tybell, C. H. Ahn, J. M. Triscone, *Appl. Phys. Lett.* **1999**, *75*, 856.
[58] S. V Kalinin, C. Y. Johnson, D. A. Bonnell, *J. Appl. Phys.* **2002**, *91*, 3816.
[59] F. Peter, K. Szot, R. Waser, B. Reichenberg, S. Tiedke, J. Szade, *Appl. Phys. Lett.* **2004**, *85*, 2896.
[60] J. Shin, V. B. Nascimento, G. Geneste, J. Rundgren, E. W. Plummer, B. Dkhil, S. V Kalinin, A. P. Baddorf, *Nano Lett.* **2009**, *9*, 3720.
[61] C. H. Ahn, K. M. Rabe, J. M. Triscone, *Science* **2004**, *303*, 488.
[62] C. H. Ahn, J. M. Triscone, J. Mannhart, *Nature* **2003**, *424*, 1015.
[63] N. Nakagawa, H. Y. Hwang, D. A. Muller, *Nat. Mater.* **2006**, *5*, 204.
[64] J. Shin, S. V. Kalinin, A. Y. Borisevich, E. W. Plummer, A. P. Baddorf, *Appl. Phys. Lett.* **2007**, *91*, 202901.
[65] N. Reyren, S. Thiel, A. D. Caviglia, L. F. Kourkoutis, G. Hammerl, C. Richter, C. W. Schneider, T. Kopp, A. S. Ruetschi, D. Jaccard, M. Gabay, D. A. Muller, J. M. Triscone, J. Mannhart, *Science* **2007**, *317*, 1196.
[66] P. Maksymovych, S. Jesse, Y. Pu, R. Ramesh, A. P. Baddorf, S. V Kalinin, *Science* **2009**, *324*, 1421.
[67] V. Garcia, S. Fusil, K. Bouzehouane, S. Enouz-Vedrenne, N. D. Mathur, A. Barthelemy, M. Bibes, *Nature* **2009**, *460*, 81.
[68] K. S. Takahashi, M. Kawasaki, Y. Tokura, *Appl. Phys. Lett.* **2001**, *79*, 1324.
[69] J. Hoppler, J. Stahn, C. Niedermayer, V. K. Malik, H. Bouyanfif, A. J. Drew, M. Rossle, A. Buzdin, G. Cristiani, H. U. Habermeier, B. Keimer, C. Bernhard, *Nat. Mater.* **2009**, *8*, 315.
[70] R. G. Moore, J. D. Zhang, V. B. Nascimento, R. Jin, J. D. Guo, G. T. Wang, Z. Fang, D. Mandrus, E. W. Plummer, *Science* **2007**, *318*, 615.
[71] U. Diebold, *Appl. Phys. A* **2003**, *A76*, 681.
[72] A. M. Kolpak, L. Dongbo, S. Rui, A. M. Rappe, D. A. Bonnell, *Phys. Rev. Lett.* **2008**, *101*, 036102 (4 pp.).
[73] G. Herranz, M. Basletic, M. Bibes, C. Carretero, E. Tafra, E. Jacquet, K. Bouzehouane, C. Deranlot, A. Hamzic, J. M. Broto, A. Barthelemy, A. Fert, *Phys. Rev. Lett.* **2007**, *98*, 216803.
[74] J. Shin, V. B. Nascimento, G. Geneste, J. Rundgren, E. W. Plummer, B. Dkhil, S. V Kalinin, A. P. Baddorf, *Nano Lett.* **2009**, *9*, 3720.
[75] J. Shin, A. Y. Borisevich, V. Meunier, J. Zhou, E. W. Plummer, S. V Kalinin, A. P. Baddorf, *ACS Nano* **2010**, *4*, 4190.
[76] K. Fuchigami, Z. Gai, T. Z. Ward, L. F. Yin, P. C. Snijders, E. W. Plummer, J. Shen, *Phys. Rev. Lett.* **2009**, 102.
[77] H. Zenia, G. Gehring, G. Banach, W. Temmerman, *Phys. Rev. B* **2005**,*71*, 024416.
[78] Z. Fang, K. Terakura, *J. Phys. Soc. Jpn.* **2001**, *70*, 3356.
[79] A. Filippetti, W. Pickett, *Phys. Rev. B* **2000**, *62*, 11571.
[80] M. Calderón, L. Brey, F. Guinea, *Phys. Rev. B* **1999**, *60*, 6698.
[81] M. Quijada, J. erne, H. D. Drew, K. H. Ahn, A. J. Millis, R. Shreekala, R. Ramesh, M. Rajeswari, T. Venkatesan, *Phys. Rev. B* **1998**, *58*, 16093.
[82] T.-H. Kim, M. Angst, B. Hu, R. Jin, X. G. Zhang, J. F. Wendelken, E. W. Plummer, A.-P. Li, *Proc. Natl. Acad. Sci. USA* **2010**, *107*, 5272.
[83] P. Popper, S. N. Ruddlesden, *Acta Cryst.* **1958**, *11*, 54.
[84] M. A. Hossain, Z. Hu, M. W. Haverkort, T. Burnus, C. F. Chang, S. Klein, J. D. Denlinger, H. J. Lin, C. T. Chen, R. Mathieu, Y. Kaneko, Y. Tokura, S. Satow, Y. Yoshida, H. Takagi, A. Tanaka, I. S. Elfimov, G. A. Sawatzky, L. H. Tjeng, A. Damascelli, *Phys. Rev. Lett.* **2008**, *101*, 16404.
[85] R. Mathieu, A. Asamitsu, Y. Kaneko, J. P. He, X. Z. Yu, R. Kumai, Y. Onose, N. Takeshita, T. Arima, H. Takagi, Y. Tokura, *Phys. Rev. B* **2005**, *72*, 92404.

[86] S. A. Grigera, R. S. Perry, A. J. Schofield, M. Chiao, S. R. Julian, G. G. Lonzarich, S. I. Ikeda, Y. Maeno, A. J. Millis, A. P. Mackenzie, *Science* **2001**, *294*, 329.
[87] R. S. Perry, L. M. Galvin, S. A. Grigera, L. Capogna, A. J. Schofield, A. P. Mackenzie, M. Chiao, S. R. Julian, S. I. Ikeda, S. Nakatsuji, Y. Maeno, C. Pfleiderer, *Phys. Rev. Lett.* **2001**, *86*, 2661.
[88] M. B. Stone, M. D. Lumsden, R. Jin, B. C. Sales, D. Mandrus, S. E. Nagler, Y. Qiu, *Phys. Rev. B* **2006**, *73*, 174426.
[89] T. H. Kim, Z. H. Wang, J. F. Wendelken, H. H. Weitering, W. Z. Li, A. P. Li, *Rev. Sci. Instrum.* **2007**, *78*, 7.
[90] T.-H. Kim, X.-G. Zhang, D. M. Nicholson, B. M. Evans, N. S. Kulkarni, B. Radhakrishnan, E. A. Kenik, A.-P. Li, *Nano lett.* **2010**, *10*, 3096.
[91] A. Moreo, S. Yunoki, E. Dagotto, *Science* **1999**, *283*, 2034.
[92] K. H. Ahn, T. Lookman, A. R. Bishop, *Nature* **2004**, *428*, 401.